Computers and Geotechnics 188 (2025) 107525

Contents lists available at ScienceDirect

Computers and Geotechnics

journal homepage: www.elsevier.com/locate/compgeo

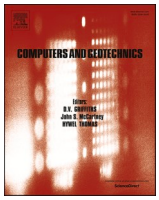

Research Paper

DEM-PFV numerical investigation of the spatial heterogeneity induced by suffusion in sands

Katia Boschi [a,*], Bruno Chareyre [b], Claudio di Prisco [a]

[a] DICA - Department of Civil and Environmental Engineering, Politecnico di Milano, Milan, Italy
[b] Univ. Grenoble Alpes, CNRS, Grenoble INP, 3SR, 38000 Grenoble, France

ARTICLE INFO

Keywords:
DEM-PFV coupling
Sands
Permeation
Intrinsic permeability
Suffusion

ABSTRACT

The permeation of Newtonian fluids through sandy soils is a crucial phenomenon in geology, environmental sciences, civil and petroleum engineering. Hydraulic conductivity is a key parameter for modelling permeation and is often assumed to be constant over time and in space, by disregarding suffusion phenomena that cause an evolution of local both grain size distribution and void ratio, due to soil mass transport/deposition processes in the porous medium.

In this paper, the problem is approached at the pore-scale, where the previously mentioned processes occur, by using the DEM-PFV coupled method (Discrete Element Method and Pore-scale Finite Volume). Although this method has been originally conceived for spherical particles, a strategy to account for particle angularity, without explicitly modelling the full geometric complexity of real sandy grains, is proposed and validated against experimental permeability test results.

The induced spatial heterogeneity and the evolution of hydraulic conductivity due to suffusion processes are then analysed by simulating erodimetric tests. An interpretative simplified approach, leveraging a state variable based on sand particle size distribution, is also suggested to predict the inception of suffusion. This state variable seems to be very useful for interpreting experimental results by (i) predicting the geometry of the final heterogeneous configuration (in terms of distance between two successive clogging zones), (ii) estimating the amount of eroded fines, and (iii) capturing the hydraulic conductivity evolution during permeation processes potentially causing suffusion.

1. Introduction

The permeation of fluids in sandy soils is a fundamental phenomenon in geology, civil and petroleum engineering, and environmental sciences. It underpins a wide range of applications, including oil and gas extraction, contaminant transport in the subsurface, design of underground geotechnical structures (Bilotta et al., 2022), and soil consolidation treatments (Boschi et al., 2023b). For Newtonian fluids, flow is commonly modelled under steady-state conditions using seepage equations, where hydraulic conductivity K, depending on both seeping fluid properties and soil intrinsic permeability k (Chapuis, 2012), plays a central role (Scheidegger, 1957; Boschi et al., 2024). K is typically assumed constant with time and, for homogeneous materials, in space (Boschi et al., 2023a).

However, this simplification breaks down when suffusion occurs—a micro-mechanical erosion process whereby seepage forces selectively detach finer particles that are not involved in load-bearing force chains (Ke and Takahashi, 2014). Not associated with either volumetric or deviatoric strains, suffusion causes local changes in particle size distribution *PSD* and void ratio e, potentially altering both hydraulic and mechanical behaviour of soils (Chang and Zhang, 2011; Ke and Takahashi, 2012). Detached fines are transported within the pore network until they re-settle, inducing local clogging (Valdes & Santamarina, 2006). In the light of the numerical results described here in the following, according to the authors, the phenomenon may be described by using characteristic internal length ℓ_c that is the distance between two adjacent clogging zones where deposition occurs.

Traditional suffusion assessment methods have been largely empirical, based on macro-scale interpretations neglecting the progressive evolution of heterogeneity within the soil specimen (Kenney and Lau, 1986; Bonelli, 2013; Kezdi, 2013; Marot et al., 2016; To et al., 2018). For instance, Sterpi (2003) proposed an exponential law at the macro-scale

* Corresponding author at: Department of Civil and Environmental Engineering (DICA), Politecnico di Milano, Piazza Leonardo da Vinci 32, 20133 Milan, Italy.
E-mail address: katia.boschi@polimi.it (K. Boschi).

https://doi.org/10.1016/j.compgeo.2025.107525
Received 24 February 2025; Received in revised form 4 July 2025; Accepted 24 July 2025
Available online 6 August 2025

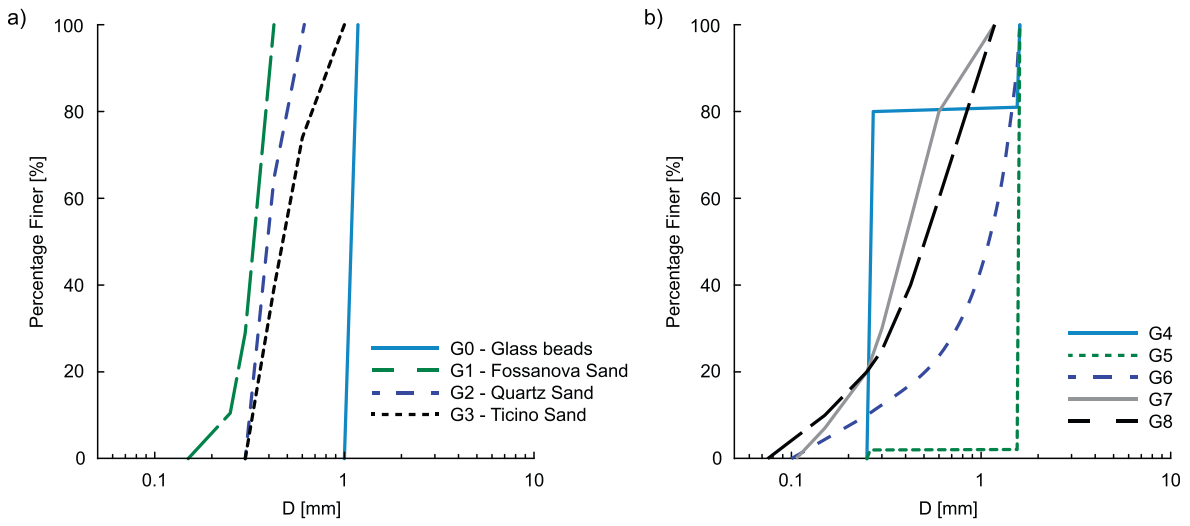

Fig. 1. a) Poorly-graded and b) widely-graded *PSD* s of granular materials.

Table 1
*PSD*s potentially susceptible to suffusion: common *PSD* coefficients (D_0, coefficient of uniformity $C_u = D_{60}/D_{10}$, gap width coefficient $W_g = \log(D_{100}/D_0)$), PoS_0 as defined in Fig. 2.

	D_0 [mm]	C_u [-]	W_g [-]	PoS_0 [-]
G4	0.25	–	0.81	−0.13
G5	0.25	–	0.81	0.53
G6	0.1	5	–	0.29
G7	0.11	2.7	–	−0.01
G8	0.075	4	–	0.13

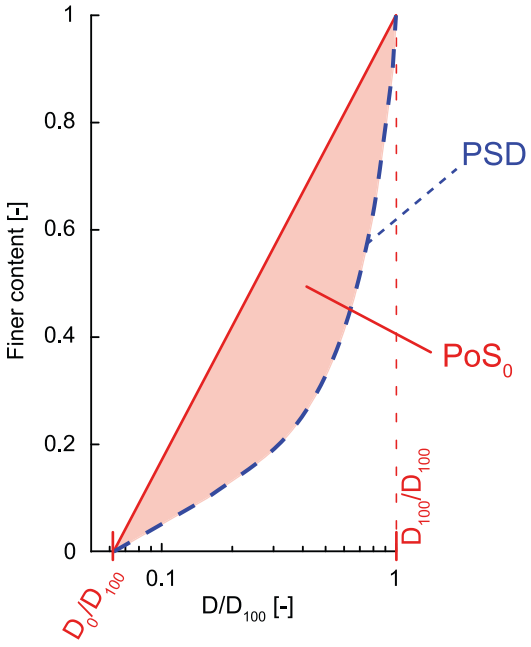

Fig. 2. Initial value of POtential to Suffusion (PoS_0) of G6 granular medium.

for the assessment of the amount of the eroded material as a function of time and hydraulic gradient. However, this approach neglects the role of ℓ_c in affecting the results, particularly with respect to their dependence on specimen's dimensions. The simultaneous occurrence of both transport and deposition/clogging at different locations within the tested specimens makes impossible to experimentally single out the two

Table 2
Micro-mechanical parameters of particles in DEM model for permeability/erodimetric tests (E the ratio of the normal contact stiffness to the particle size, ν_p the ratio of the tangential to the normal contact stiffnesses, μ_p the inter-particle friction coefficient, α_r the rolling stiffness coefficient and η_r the rolling friction coefficient; Hosn et al., 2017) and ρ_s particles' density.

	E [MPa]	ν_p [-]	μ_p [-]	α_r [-]	η_r [-]	ρ_s [kg/m^3]
Glass Beads	40k	0.22	0.2	0.0	0.0	2550
Sands	200	0.2	0.46	7.5	0.22	2650

contributions on the basis of the amount of fine particles leaving the specimen over time.

In recent years, numerical modelling based on discontinuum approaches has emerged as a powerful tool to explore suffusion mechanisms. Many studies have adopted unresolved DEM-CFD approaches (e.g., Hu et al., 2019; 2020; Chen et al., 2023b; Cao et al., 2024), where, however, the mesh size of the fluid grid is coarser than both fine and coarse particles. The flow field is then volume-averaged within a local space by solving the locally averaged Navier-Stokes equation and fluid–particle interactions estimated by means of empirical methods. These limitations then prevent an accurate capture of the local flow dynamics at particle–fluid interfaces, particularly during detachment and transport of fines (Chen et al., 2022; Liu et al., 2023). Only recently, fully resolved DEM-CFD methods have been employed by Chen et al. (2022) and Liu et al. (2024), but these works have focused on different aspects—the onset of erosion processes involving also load-bearing particles and the effect of particles' shapes and orientations during suffusion, respectively—providing a global validation rather than a direct insight into the aspects addressed here.

In this study, the authors adopt a different numerical framework to accurately model suffusion-related processes at the pore scale: the DEM–PFV coupling (Discrete Element Method – Pore-scale Finite Volume). Owing to the method, ensuring computational efficiency in terms of time and memory usage, the two-way fluid–solid coupling is simulated (Catalano et al., 2014). The method is particularly suited for modelling fluid-driven particle transport, capturing the effect of local pore geometry and connectivity on both force distribution and flow pathways. The DEM–PFV scheme implemented in YADE (Smilauer et al., 2023; Angelidakis et al., 2024), developed by Chareyre et al. (2012), is here used to simulate laminar viscous flows through sandy specimens composed of spherical grains.

The micro-mechanical potential of this approach in stress- and flow-driven erosion scenarios was first demonstrated by Wautier et al. (2019).

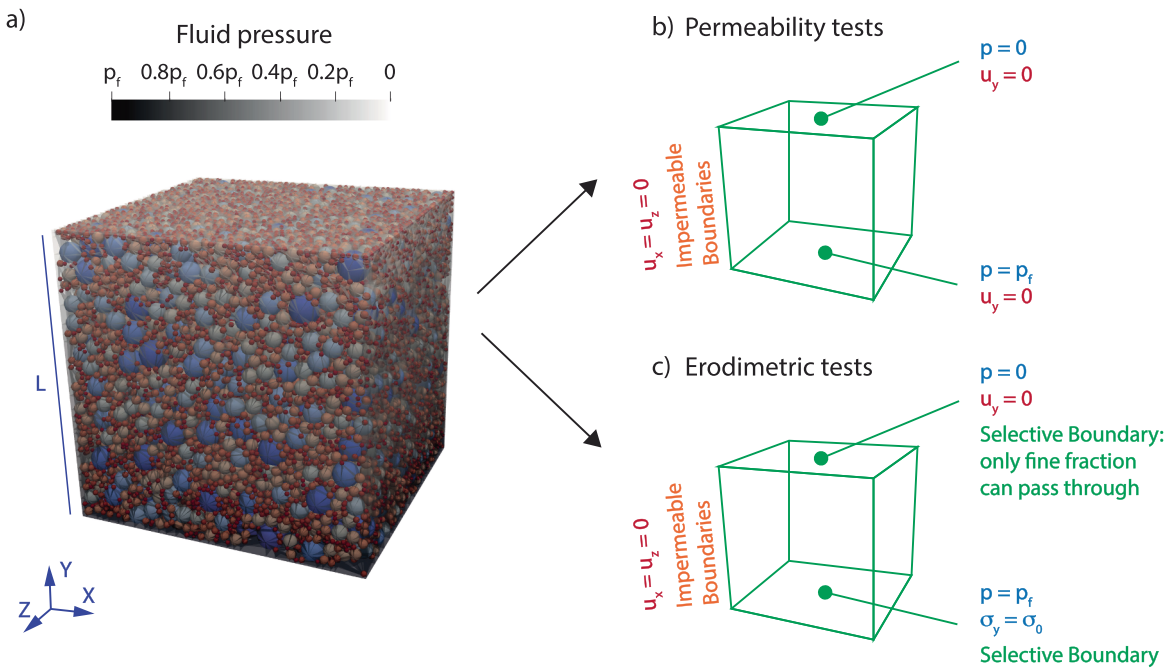

Fig. 3. A) DEM-PFV numerical model; imposed boundary conditions for b) permeability tests and c) erodimetric tests. For the sake of representation clarity, the system of reference is rotated of 90°.

Table 3
Void ratio e_0 of the examined specimens, specific surface area S_0 of the investigated granular media (*PSD* s in Fig. 1a), and α parameter.

	e_0[-]	S_0[mm^{-1}]	$\alpha = S^2_{0,DEM}/S^2_0$[-]
G0 – Glass beads	0.56	5.717	0.9
G1 – Fossanova sand	0.80	26.414	0.52
G2 – Quartz sand	0.76	21.140	0.44
G3 – Ticino sand	0.78	22.035	0.35

Building upon that, the present work introduces several new contributions. Specifically,

- the influence of sand particles' angularity on intrinsic permeability assessment is discussed (§4) and a numerical strategy to account for particle angularity in DEM-PFV simulations proposed (§5);
- suffusion-related processes investigated at a local scale and their evolution described (§5);
- a novel interpretative framework to support suffusion prediction in engineering applications introduced in §2 and discussed in §6;
- the impact of suffusion on soil hydraulic behaviour assessed (§6).

As for suffusion processes, the main innovation of this study lies in interpreting them at a *meso*-scale smaller than the specimen dimensions, enabling a theoretical understanding of particle transport and deposition mechanisms. This is achieved through the definition of two original variables: POtential to Suffusion *PoS* and the previously mentioned characteristic length ℓ_c, aiming to improve the predictability of suffusion onset and effects.

2. Predicting potential to suffusion in sands

Particle size distributions (*PSDs*) of sands are expected to be fundamental in governing the occurrence of suffusion (Kézdi, 2013; To et al., 2018). According to filter criteria (Kenney & Lau, 1986), suffusion occurs in graded materials, where the coarse fraction of the *PSD* acts as a filter with respect to finer particles (referred to as fines), susceptible to migration under seepage flow. In this Section, the authors (i) define a state variable related to current *PSD*, hereinafter named *PoS* (POtential to Suffusion), and (ii) provide an initial insight into how the *PoS* value relates to the occurrence of suffusion. The purpose is to offer the reader a preliminary understanding of the study's rationale and direction, while the detailed discussion and justification of the *PoS* and its threshold value are provided later in §6.

The *PSDs* of the sands herein numerically investigated are reported in Fig. 1. In particular, the poorly graded *PSDs* (G0, G1, G2 and G3) are illustrated in Fig. 1a, whereas, the more widely graded *PSDs* (G4, G5, G6, G7 and G8; Table 1), i.e. those potentially susceptible to suffusion, in Fig. 1b. G4 and G5 are characterised by a bi-dispersed *PSD*, with the same D_0 and D_{100} (with D_X the diameter corresponding to X% of the passing mass fraction), whereas G6, G7 and G8 by continuously-graded *PSDs*.

In this paper, the authors aim at demonstrating that the variable governing the inception of suffusion under homogeneous conditions in granular media is the initial value of *PoS* (PoS_0; Table 1), defined as the non-dimensional area schematised in Fig. 2: area between the *PSD* curve under exam (blue dotted line) and the straight line intersecting it at D_0 and D_{100} (red solid line). It is worth noticing that this study is limited to sandy soils, where also D_0 can be accurately determined through standard particle size distribution techniques.

As will be numerically demonstrated in §5, for positive PoS_0 values, suffusion occurs giving rise to a local evolution of *PSD* as well as of *e*. Moreover, according to filters' theories, the current local *PoS* value will be discussed not to be the only variable governing the subsequent evolution of suffusion. Indeed, in heterogenous systems, the spatial gradient of *PoS* plays a significant role, either inhibiting or enhancing suffusion.

3. Numerical modelling

In this Section, after a brief description of the employed DEM-PFV coupled method (§3.1), the authors illustrate the DEM specimen preparation technique adopted (§3.2) and the numerical tests performed: permeability (§3.3) and erodimetric (§3.4) tests, differing from each other for the boundary conditions imposed.

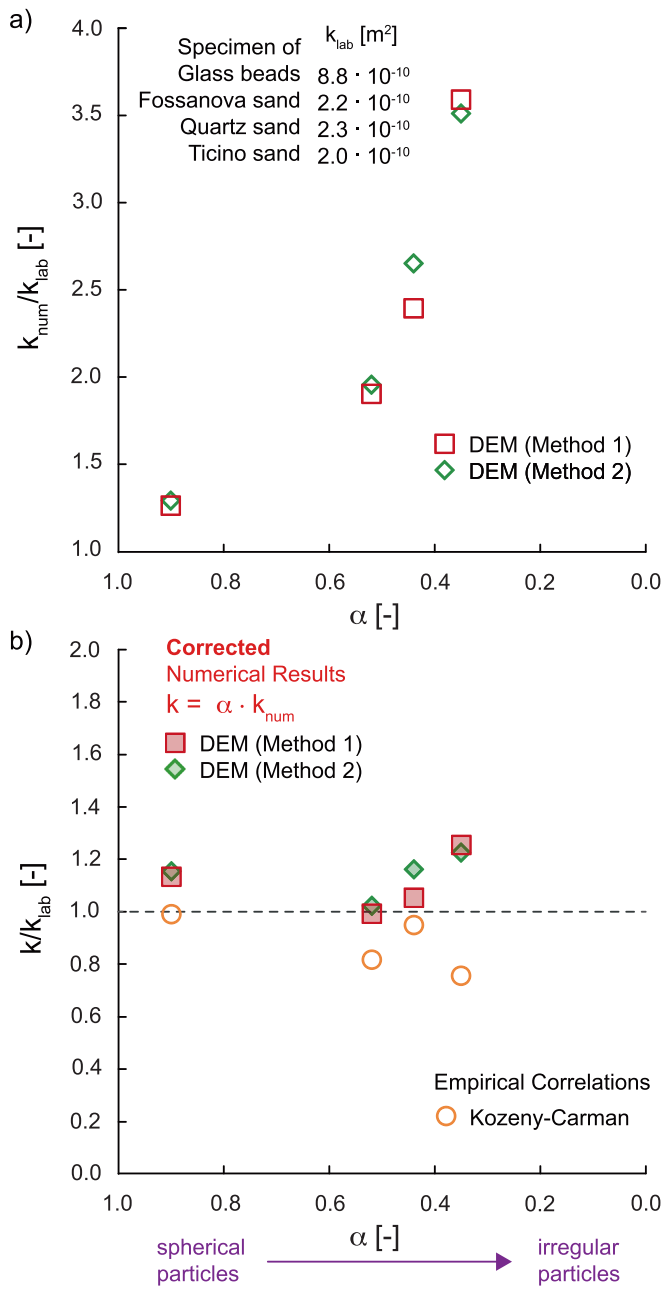

Fig. 4. Intrinsic permeability k of the investigated granular media: comparison between a) numerical k_{num} and experimental k_{lab} results, b) corrected numerical and experimental results with results derived from Kozeny-Carman correlation.

Table 4
Erodimetric tests performed ($e_{max,Gi}$ reported in Table 5).

Tests	upon	e_0 [-]	σ_0 [kPa]	μ_f [mPa·s]	Δp [kPa]
T0	G4, G5, G6, G7, G8	$e_{max,Gi}$	5	1	0.3
T1	G6	0.57	500	1	0.3
T2	G6	$e_{max,G6}$	5	5	0.3
T3_0	G6	$e_{max,G6}$	5	1	0.1
T3_1	G6	$e_{max,G6}$	5	1	4.8k

3.1. DEM-PFV coupled method

The Discrete Element Method (DEM; Cundall and Strack, 1979), extensively used in literature to study, at the micro-scale, the mechanical behaviour of granular media (Scholtes et al., 2009), is essentially a

Table 5
Maximum void ratio e_{max} for *PSD* Gi with $i = 4,8$, denoted as $e_{max,Gi}$.

	G4	G5	G6	G7	G8
e_{max} [-]	0.69	0.86	0.59	0.67	0.58

Lagrangian technique, according to which each particle is assumed to be a rigid body whose interaction with the others is described by a suitable contact law. In particular, the numerical results illustrated in this paper are obtained by assuming sand grains to be spherical and employing the contact law proposed by Hosn et al. (2017), according to which: (i) along the normal direction to the contact plane, a simple bi-linear elastic contact law is adopted, (ii) along the tangential direction, a linear elastic spring is set in series with a frictional slider obeying Coulomb's law and (iii) rolling resistance is included to overcome excessive rolling that may occur between spherical particles. For each computation time step, interaction forces/moments among particles are derived from spheres' positions by means of contact laws. Then, the new spheres' positions are computed by integrating the Newton's second law according to an explicit second-order finite difference scheme and accounting for interparticle forces, volume and superficial forces.

With reference to 2D models of disc assemblies, Hakuno (1995) and later Bonilla (2004) firstly proposed to couple DEM with a pore-network method to simulate interstitial fluid flows. Then, Chareyre et al. (2012) adapted this approach to 3D granular packings. This goal has been achieved by using a pore-scale discretization in finite volumes (PFV) in which incompressible Newtonian pore fluids are assumed to flow in a laminar regime.

In the PFV method, a regular Delaunay triangulation is used to partition the three-dimensional geometry of the void space: the void space being discretized by tetrahedra with spheres at each vertex. Analogously, the dual Voronoi network represents the connections/paths of the fluid between adjacent pores. According to this method, the fluid pressure can be calculated, once velocity field of particles is known, by assuming fluid pressure p to be constant in each pore and by imposing the balance of mass in each pore i of volume V_i^f. Such a mass balance equation is governed by the relative position of grains and by the flux of water q_{ij} passing through the constrictions (of facet S_{ij}^f) joining two adjacent pores (from pore i to pores j):

$$\dot{V}_i^f = -\sum_{j=j_1}^{j_4} q_{ij} \tag{1}$$

where $\dot{}$ stands for time derivative. Equation (1) is then integrated by imposing:

- the compatibility equation that couples the deformation of the solid skeleton with the fluid flow:

$$\dot{V}_i^f = \sum_{j=j_1}^{j_4} \int_{S_{ij}^f} (v_n - u_n)\, ds \tag{2}$$

where v_n and u_n stands for the normal components of DEM particle and fluid velocities, respectively;

- the Stokes equation that predicts a linear relationship between the fluid velocity and the pressure gradient:

$$q_{ij} = g_{ij}\left(\mu_f\right) \frac{p_i - p_j}{l_{ij}} \tag{3}$$

where g_{ij} is the local conductance factor of the associated facet, also a function of Newtonian fluid viscosity μ_f, and l_{ij} is the interpore distance. The accuracy of the PFV model relies on suitable definitions of these two parameters based on the local geometry of constrictions (Chareyre et al.,

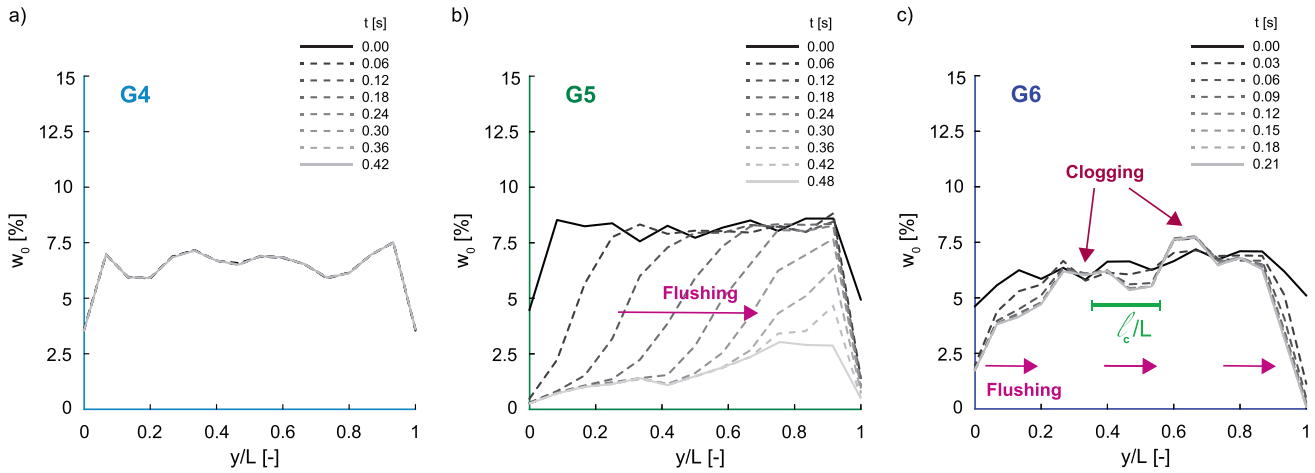

Fig. 5. Spatial distribution with time of w_0, that is the weight of all the fine particles (characterised by a diameter D so that $D \leq D_{10}$) located in a y-range with respect to the overall weight of the fine particles: a) G4, b) G5 and c) G6 employed in test T0.

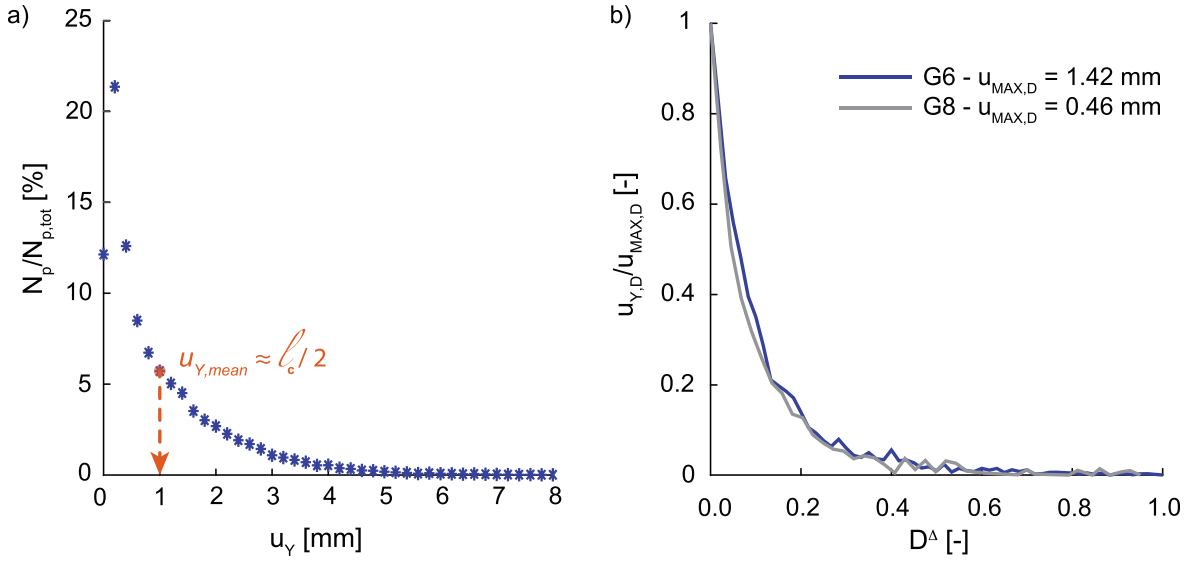

Fig. 6. Test T0: a) G6 case, distribution of particle cumulative displacements along y direction u_Y once reached the new steady-state condition (N_p stands for particles' number and $N_{p,tot}$ total particles' number); b) mean particle cumulative displacement along y direction $u_{Y,D}$ normalised by $u_{MAX,D}$ as a function of diameter $D^\Delta = \frac{D-D_0}{D_{100}-D_0}$.

2012).

As well as particle velocity through Equation (2) affects the resolution of the hydraulic problem, the solution of the mechanical problem (DEM computation) is affected by superficial forces F_f^k transmitted by the flowing fluid to particles (hydro-mechanical coupling):

$$F_f^k = \int_{d\Gamma_k} (p\,\boldsymbol{n} + \boldsymbol{\tau}\,\boldsymbol{n})\,ds \tag{4}$$

where F_f^k is the total fluid force acting on particle k, $\int_{d\Gamma_k} ds$ the integral along the contour of particle k, $\boldsymbol{n}$ the unit normal of the particle contour, $\boldsymbol{\tau}$ the viscous shear stress (Chareyre et al., 2012).

At each time step, V_i^f is computed (Equation (2), then, by means of Equations (1) and (3), the pressure field is obtained, and, according to Equation (4), new fluid forces calculated and integrated into the conventional time-stepping algorithm of the DEM summing them with the contact forces.

The accuracy and reliability of the DEM-PFV method, as implemented in Yade, have been thoroughly validated in previous studies (Catalano et al., 2011; Chareyre et al., 2012). A very good agreement between numerical predictions and experimental data on permeability measurements in glass bead samples has been reported by Tong et al. (2012), and further confirmed in §4 of the present work. Following the approach proposed by Zhong et al. (2018), the numerical tool was also validated in terms of cumulative eroded mass versus cumulative expended energy in Boschi (2021), where dedicated erodimetric tests were designed in lab to replicate the numerical setup also adopted in this study.

3.2. DEM specimen preparation

The DEM specimen is herein prepared under dry conditions. Two different procedures are adopted: the former one (Method 1) is conceived to reproduce the experimental specimens also tested in the lab (§4), whereas the latter one (Method 2) is standard and the specimens obtained are characterised by an ideal and not specific micro-structure.

Method 1 is characterised by three subsequent phases, one experimental and two numerical. During Phase 1, a sand specimen is prepared in the lab and a cubic portion CP (of about 6 cm^3) in the middle of it is

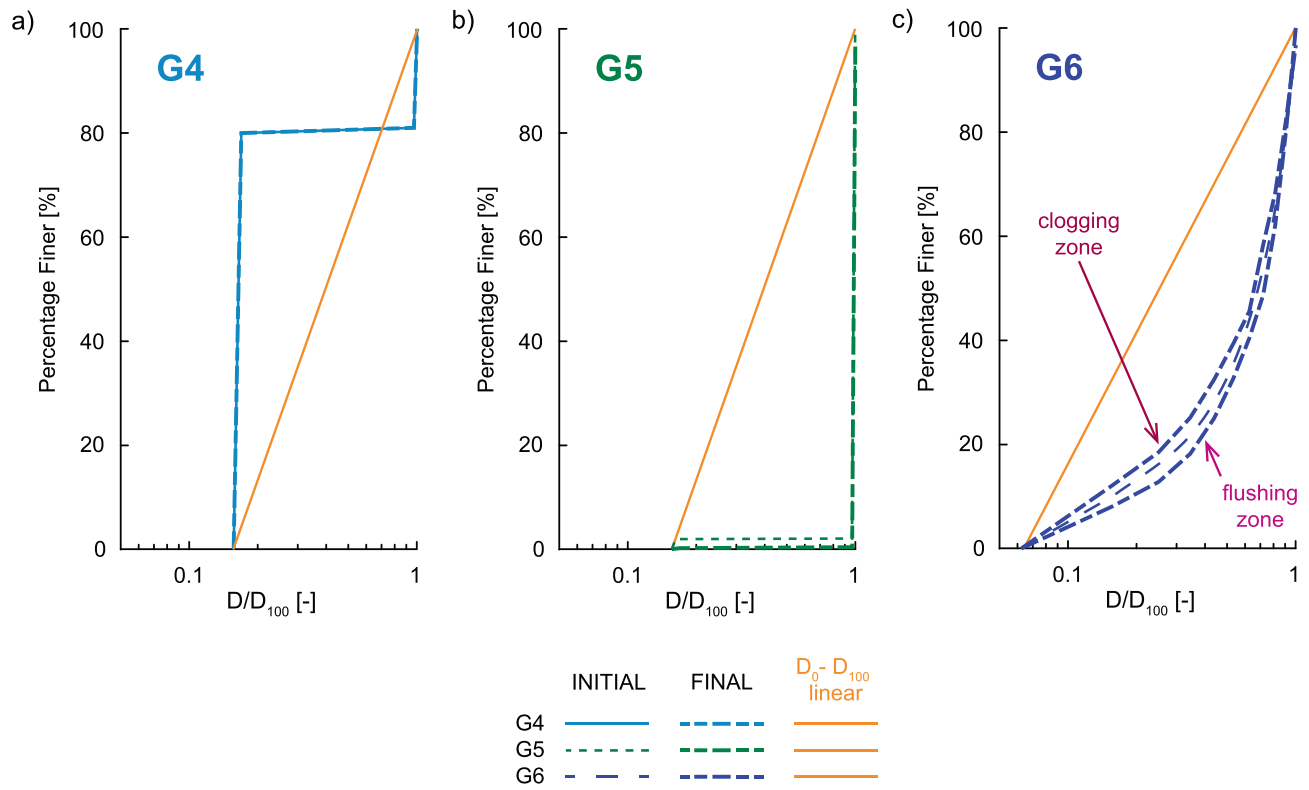

Fig. 7. Comparison between initial *PSD* and correspondent *PSD* at the end of the erodimetric test: a) G4, b) G5 and c) G6 employed in test T0.

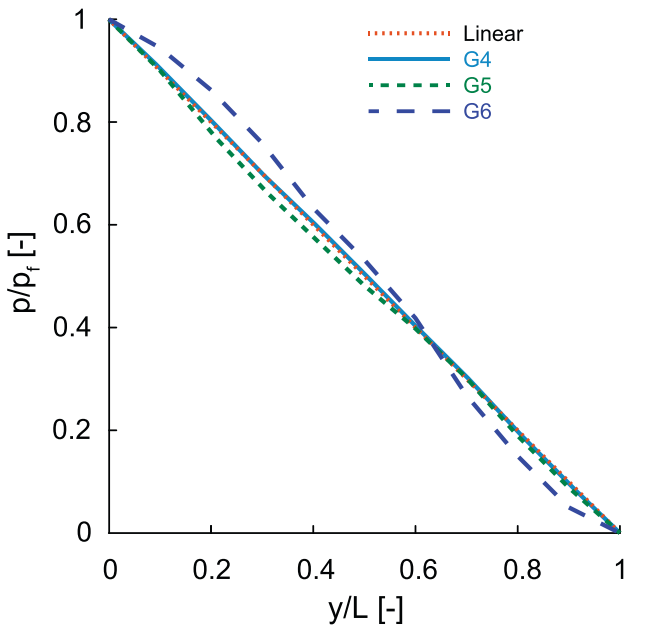

Fig. 8. Spatial distribution of p along the flow direction once reached the new steady-state: G4, G5 and G6 employed in test T0.

scanned by using a tomography procedure (Appendix A). During Phase 2, CP is reproduced via DEM and surrounded by fixed rigid walls. Spheres, characterised by the same volume-equivalent radius and located in the same relative position of particles in CP, are generated and a value for inter-particle friction coefficient equal to μ_p assigned. On the boundaries of the DEM specimen, the desired isotropic stress value σ_0 is imposed and kept constant during Phase 3, by means of a servo-controlled mechanism (regulating step-by-step the boundaries' displacements, with the aim of ensuring the application and the maintenance of the target stress value). Phase 3 lasts until the system reaches 'static' conditions, which are conventionally achieved when unbalanced non-dimensional forces are lower than 10^{-5} (defined as the ratio of maximum resultant particle force modulus over mean contact resultant force modulus). As for the employment of Method 1, it is worth noticing that, during Phase 2, no so significant overlaps or unintended separations among DEM particles that could compromise the stability of the sample were observed and, during Phase 3, "static" conditions were reached rapidly without noticeable displacement of the boundaries. This behaviour can be attributed to the relatively regular shape of the sand grains considered in this study, where the equivalent diameter does not deviate significantly from the actual particle dimensions (aspect ratio $AR \approx 1$). Moreover, the servo-controlled mechanism applied immediately after particles' generation allows to adjust any minor overlaps or gaps, ensuring that the sample reaches a mechanically stable configuration.

Method 2 is characterised by three subsequent phases. During Phase 1, a loose cloud of non-overlapping spheres characterised by a prescribed *PSD* is generated inside a cubic domain surrounded by rigid walls. The prescribed void ratio is obtained by imposing $0 < \mu_p^* < \mu_p$, where μ_p^* is the current inter-particle friction coefficient during the specimen generation and μ_p inter-particle friction coefficient employed during the test. During Phase 2, the specimen is isotropically compressed at a sufficiently small strain rate until an isotropic stress value of 2 kPa. The 2 kPa isotropic stress value is then kept constant by means of a servo-controlled mechanism until 'static' conditions are reached. During Phase 3, after assigning a value for inter-particle friction coefficient equal to μ_p, the specimen is isotropically compressed by imposing a very small strain rate until the desired value of isotropic stress σ_0 is got.

In both cases, DEM specimens, at the end of the preparation, are verified to be homogeneous (with a constant void ratio e_0) and isotropic in terms of both stresses and fabric tensor (O'Sullivan, 2011).

The employed micro-mechanical parameters (Table 2) (i) in case of

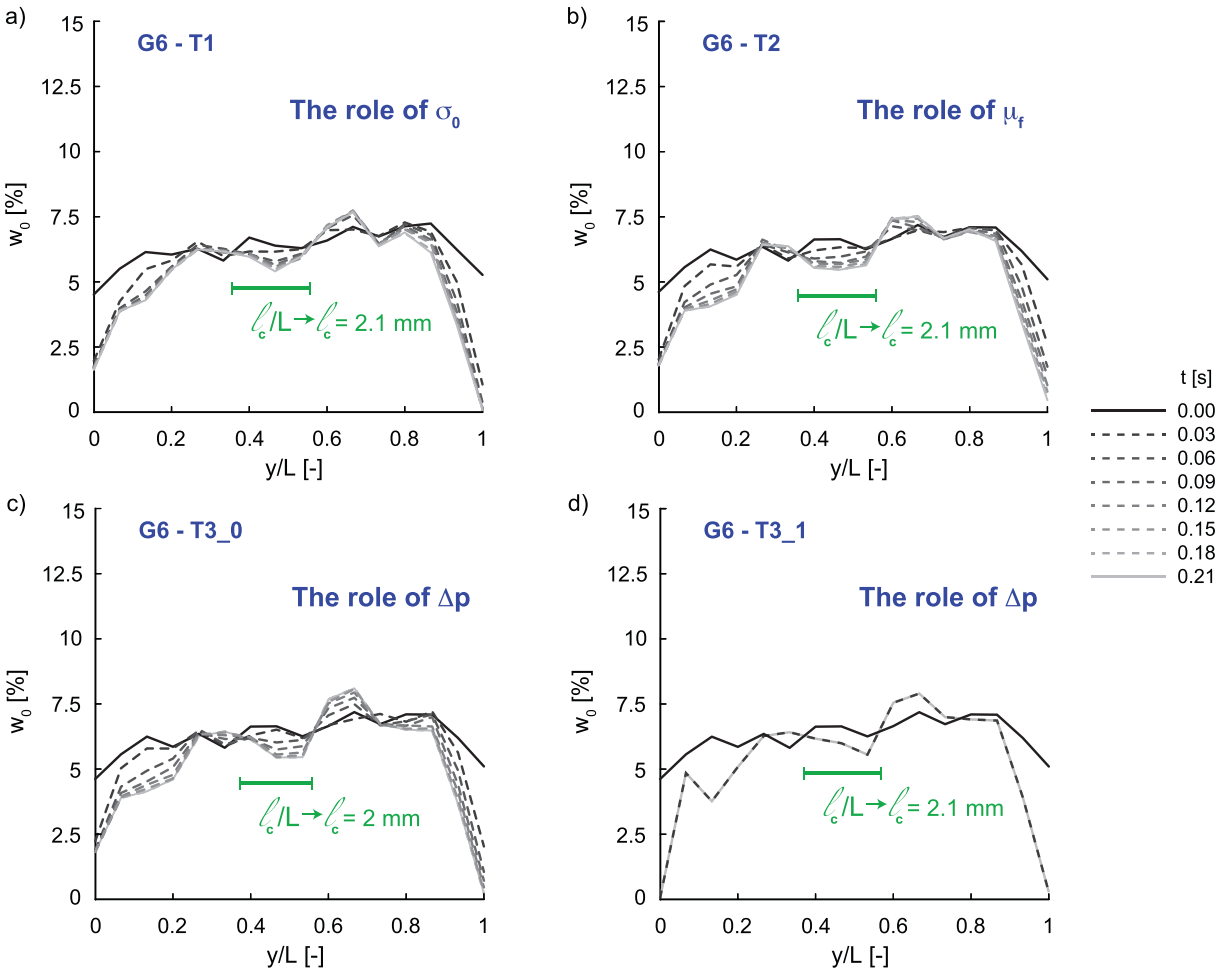

Fig. 9. Spatial distribution in time of w_0, that is the weight of all the fine particles (characterised by a diameter D so that $D \leq D_{10}$) located in a y-range with respect to the overall weight of the fine particles: G6 employed in test a) T1, b) T2, c) T3_0 and d) T3_1.

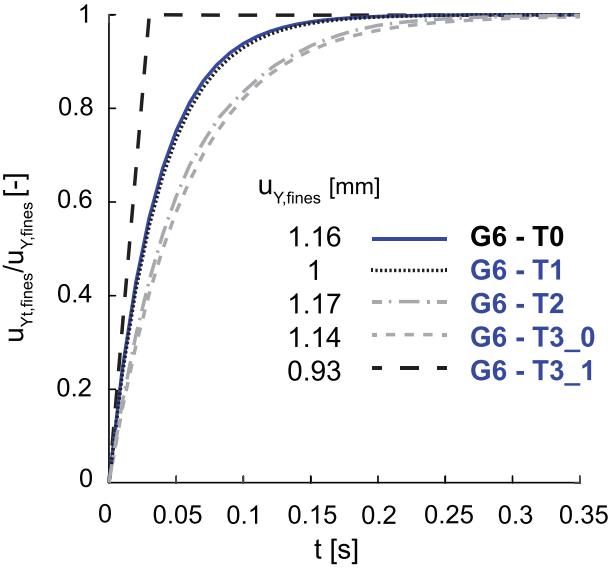

Fig. 10. G6 employed in tests T0, T1, T2, T3_0 and T3_1: temporal evolutions of fine particles' mean travelled distance along y direction $u_{Yt,fines}$ (particles such that $D \leq D_{10}$).

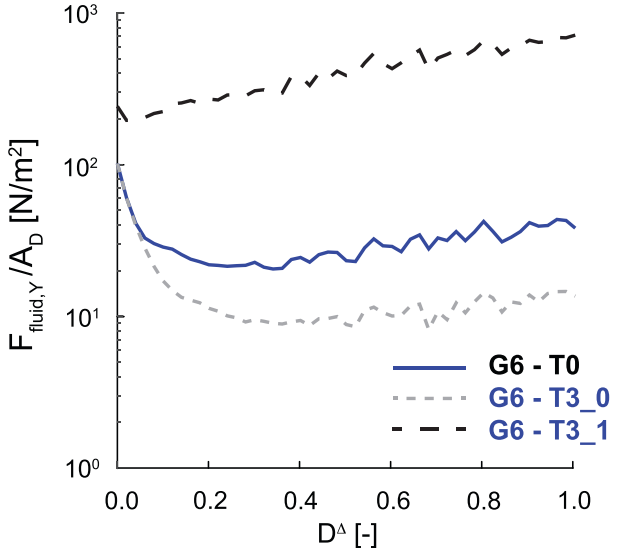

Fig. 11. G6 employed in different tests T0, T3_0, T3_1: mean $F_{fluid,Y}/A_D$ distributions at the final steady-state configurations.

sands, coincide with the ones calibrated by Hosn et al. (2017) for the simulation of natural sand via DEM using spherical particles, and employing a contact law coinciding with the one of the present study,

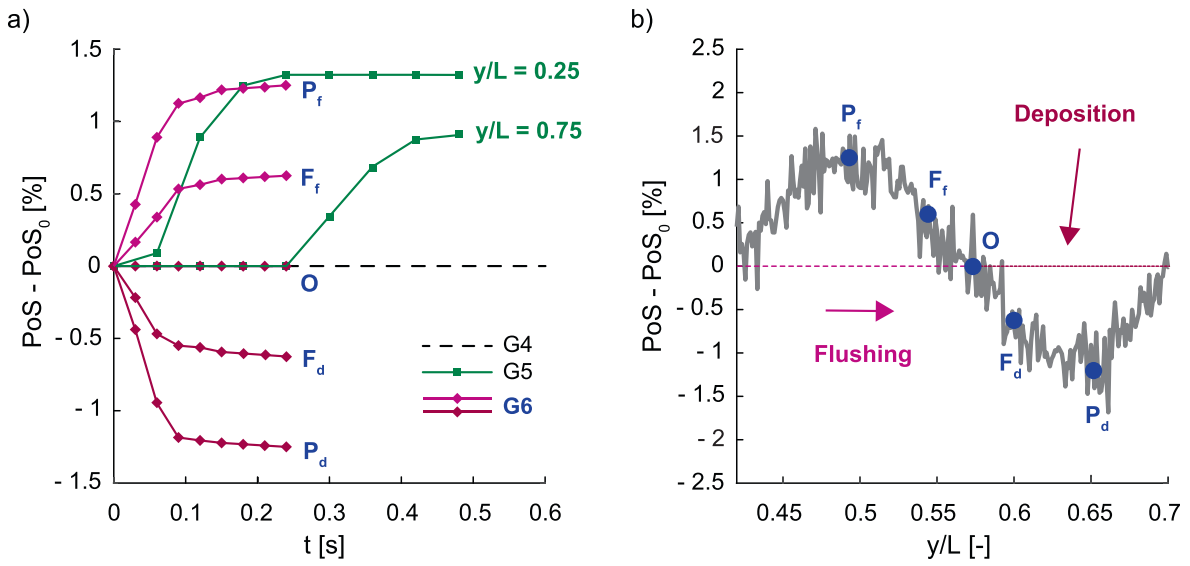

Fig. 12. A) $PoS - PoS_0$ temporal evolution in G4, G5 and G6 during T0 test (at different y/L) and b) $PoS - PoS_0$ spatial distribution in G6 at the final steady state configuration (points P_f, F_f, O, F_d and P_d are the ones taken in a) for G6).

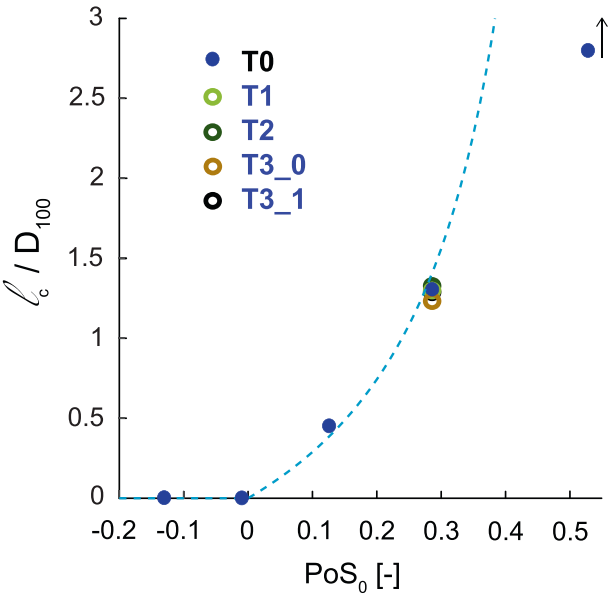

Fig. 13. Normalised characteristic length ℓ_c (ℓ_c/D_{100}) versus initial POtential to Suffusion PoS_0.

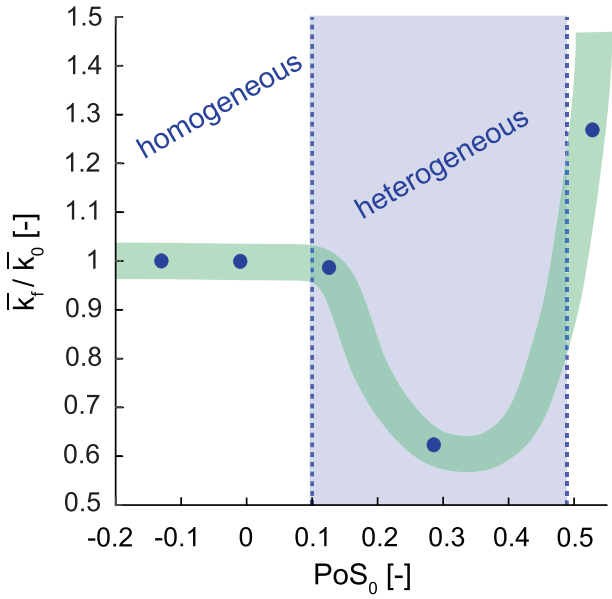

Fig. 14. T0 test case: $\bar{k}_f/\bar{k}_0$ ratio versus PoS_0.

and (ii) for glass beads, are inspired by those employed by Suhr and Six (2016) with nil rolling both stiffness and friction, since grains in this case are assumed to be ideally spherical.

3.3. DEM-PFV model for permeability tests

Permeability tests are performed (i) on specimens obtained by using both Method 1 and Method 2, (ii) after imposing $\sigma_0 = 2$ kPa and (iii) assuming pores filled with a fluid of $\mu_f = 1$ mPa·s. In Fig. 3a, the employed DEM-PFV model is schematised, whereas, in Fig. 3b, imposed boundary conditions are indicated. All the rigid boundaries are kept fixed. Boundaries with normal parallel to z and x axes are imposed to be impervious, whereas $p = p_f$ for $y = 0$ and $p = 0$ for $y = L$. The number of spheres employed, that is 15k, is sufficient to avoid dependence of K on specimen size and boundary effects.

3.4. DEM-PFV model for erodimetric tests

Erodimetric tests are performed (i) on specimens obtained by using Method 2, and (ii) assuming pores filled with a fluid of μ_f varying from test to test. In Fig. 3a, the employed DEM-PFV model is schematised, whereas, in Fig. 3c, imposed boundary conditions are indicated. All the rigid boundaries are kept fixed during the test, except for the one corresponding to $y = 0$, on which total stress $\sigma_y = \sigma_0$ is imposed. As far as hydraulic conditions are concerned, boundaries with normal parallel to z and x axes are imposed to be impervious, whereas along y direction, $p = p_f$ for $y = 0$ and $p = 0$ for $y = L$.

The two boundaries along y direction are selective: only DEM spheres with diameters $D < D_{30}$ can pass through them. This choice derives from the results of trial numerical simulations showing that suffusion mainly engages particles with $D < D_{30}$ and allows to minimize boundary effects. Particles crossing $y = L$ plane constitute the eroded fine fraction and are excluded from the numerical triangulation (§3.1). In these tests, dealing

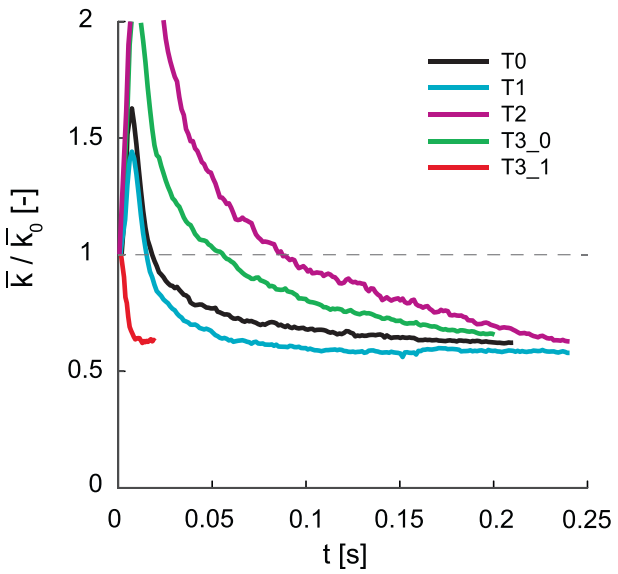

Fig. 15. Temporal evolution of $\bar{k}/\bar{k}_0$ during erodimetric tests upon G6 specimens.

with widely-graded *PSD* s (Fig. 1b), a considerably large number of spheres (50 k) is required to avoid specimen size effects: the *x*, *y* and *z* specimen dimensions are higher than $10 \bullet D_{100}$ (D_{100} denotes the largest particle diameter in the specimen).

4. Discussion on the assessment of *k*

In this Section, thanks to the comparison with 1D experimental permeability test data, the reliability of DEM-PFV numerical results in describing flows of fluids throughout porous media is discussed in relation to the assessment of *k* for glass beads and sands. In the light of the herein discussion, a simplified method for numerically accounting for the role played by sand particles' angularity is then proposed in §5.

After employing spherical glass beads as a limit case, three different sands (Fossanova, quartz, and Ticino) are considered. These sands are characterized by an aspect ratio $AR \approx 1$, increasingly irregular particle angularities, and the poorly graded PSDs shown in Fig. 1a — and are therefore not affected by suffusion phenomena. For each of them, a homogeneous lab specimen is prepared (each one characterised by a prescribed void ratio e_0 value; Table 3). Each specimen is scanned by using a micro-CT device. An accurate image post-processing (Appendix A) is used to determine soil (i) particles' positions, (ii) particles' volume-equivalent diameters and (iii) specific surface area S_0 (defined as the ratio of surface area to bulk volume; Table 3). On the basis of these data, numerical specimens are created by means of Method 1 as long as Method 2 (§3.2). Given the hypothesis of sphericity of particles, the specific surface areas of correspondent DEM specimens $S_{0,DEM}$ differ from S_0 lab values and $\alpha = S^2_{0,DEM}/S^2_0$ parameter is introduced (Table 3).

Constant head permeability tests with water are performed experimentally and reproduced numerically with the approaches mentioned in §3.3. During the tests, the mean value of the water pressure gradient is imposed and flow rate *Q* at the outlet monitored. Hydraulic conductivity *K* is then calculated, according to Darcy's law (Darcy, 1856), and intrinsic permeability *k* derived ($k = K \bullet \mu_w/\gamma_w$, where μ_w is the viscosity and γ_w the weight per unit volume of water). In Fig. 4a, experimental data (k_{lab}) are compared as a function of α with numerical results (k_{num}), obtained by using the two different specimen generation methods (red squares and green rhombuses refer to Method 1 and Method 2, respectively). The numerical results demonstrate that in case the laboratory specimen geometry is precisely reproduced, as it is in the case of glass beads ($\alpha \approx 1$) and Method 1, $k_{num}/k_{lab} \approx 1$. Even if the numerical spatial configuration of glass beads dos not perfectly coincide with lab ones (Method 2), $k_{num}/k_{lab} \approx 1$. Conversely, when $\alpha < 1$ (natural sands), the numerical prediction largely overestimates the experimental data. Indeed, as is suggested by Kozeny-Carman formula (Kozeny, 1927; Carman, 1937; Wyllie & Gardner, 1958a; 1958b), in which S_0^2 term is present, such a discrepancy is due to sand grains' angularity, causing an increase in tortuosity and energy dissipation during seepage.

In analogy with Kozeny-Carman formula, the authors herein suggest evaluating *k*, in case of sandy soils, by multiplying k_{num} by α, function of the real material's angularity of particles. To confirm the reliability of the method proposed, in Fig. 4b, αk_{num} is compared not only with k_{lab}, but also with the value of *k* evaluated according to Kozeny-Carman correlation.

5. Micro-mechanical discussion of suffusion

Experimental and numerical tests performed in §4 to evaluate *k* are characterised by initial homogeneous specimens and constant with time boundary conditions imposed. Values of *k* are also constant with time and in space, since the material microstructure does not evolve, suffusion is absent, inhibited by the poorly-graded *PSD* considered. In this Section, the numerical results of DEM-PFV erodimetric tests (§3.4; Table 4) are illustrated. Even in this case, initial homogeneous specimens and constant with time boundary conditions are employed. However, since *PSD* s (Fig. 1b) are widely-graded, the material microstructure evolves with time due to the occurrence of suffusion processes. The duration is not constant, since the test is arrested when a new steady condition is reached and suffusion processes stop. In particular, the role of *PSD*, σ_0, μ_f and Δp ($\Delta p = p_f - 0$, i.e. the difference between the *p* values imposed at the two boundaries along *y* direction) in affecting suffusion and its temporal evolution is discussed.

Additionally, it is worth noting that, in the light of the conclusions drawn in §4, a numerical strategy to account for particle angularity in DEM-PFV and accurately compute the dissipated energy consists in replacing μ_f in Equation (3) with a fictitious viscosity value, defined as μ_f/α. The validation of the approach is discussed in Appendix B by comparing the suffusion processes' rates numerically obtained by Liu et al. (2024), via the use of a DEM-CFD code in case of irregularly shaped particles, with those derived by using the approach herein proposed.

5.1. The role of *PSD*

As was previously mentioned, when suffusion takes place, the problem becomes time dependent and, as will be put in evidence in this Section, the specimen becomes heterogenous. Suffusion takes place when the hydraulic perturbation makes the micro-structural configuration of the material mechanically unstable, whereas suffusion stops when a new stable heterogeneous configuration is reached (§6).

To clarify the concepts introduced hereinabove, numerical results for 3 different specimens (G4, G5 and G6 *PSDs* in Fig. 1b) tested with test T0 of Table 4 are discussed. G4 is representative of a bi-dispersed *PSD* with a high content of fines, G5 of a bi-dispersed *PSD* with a low content of fines and G6 a continuously-graded *PSD* with a C_u value comparable with W_g of G4 and G5. In Fig. 5, the temporal evolution of fines' distribution (that is $w_0 = \frac{w_f(y/L)}{\frac{1}{L}\bullet\int_0^L w_f(y/L)dy}$, where $w_f(y/L)$ is the weight of particles characterised by $D \leq D_{10}$) is shown.

The G4 specimen ($L \cong 22$ mm) turns out not to be affected by suffusion (Fig. 5a). Indeed, in G4, the pore matrix cannot be travelled by the fine fraction, involved in the solid skeleton ($Z \cong Z_m \cong 4$, with *Z* and Z_m the overall and the mechanical coordination number, respectively).

In contrast, in case of G5 ($L \cong 23.5$ mm), the fine fraction is almost fully transported by the flux throughout pores (Fig. 5b), since most fine particles in G5 are initially rattlers, i.e. particles not in contact with their neighbours (initially, $Z \leq 1$, whereas $Z_m \cong 4$), but not all particles are

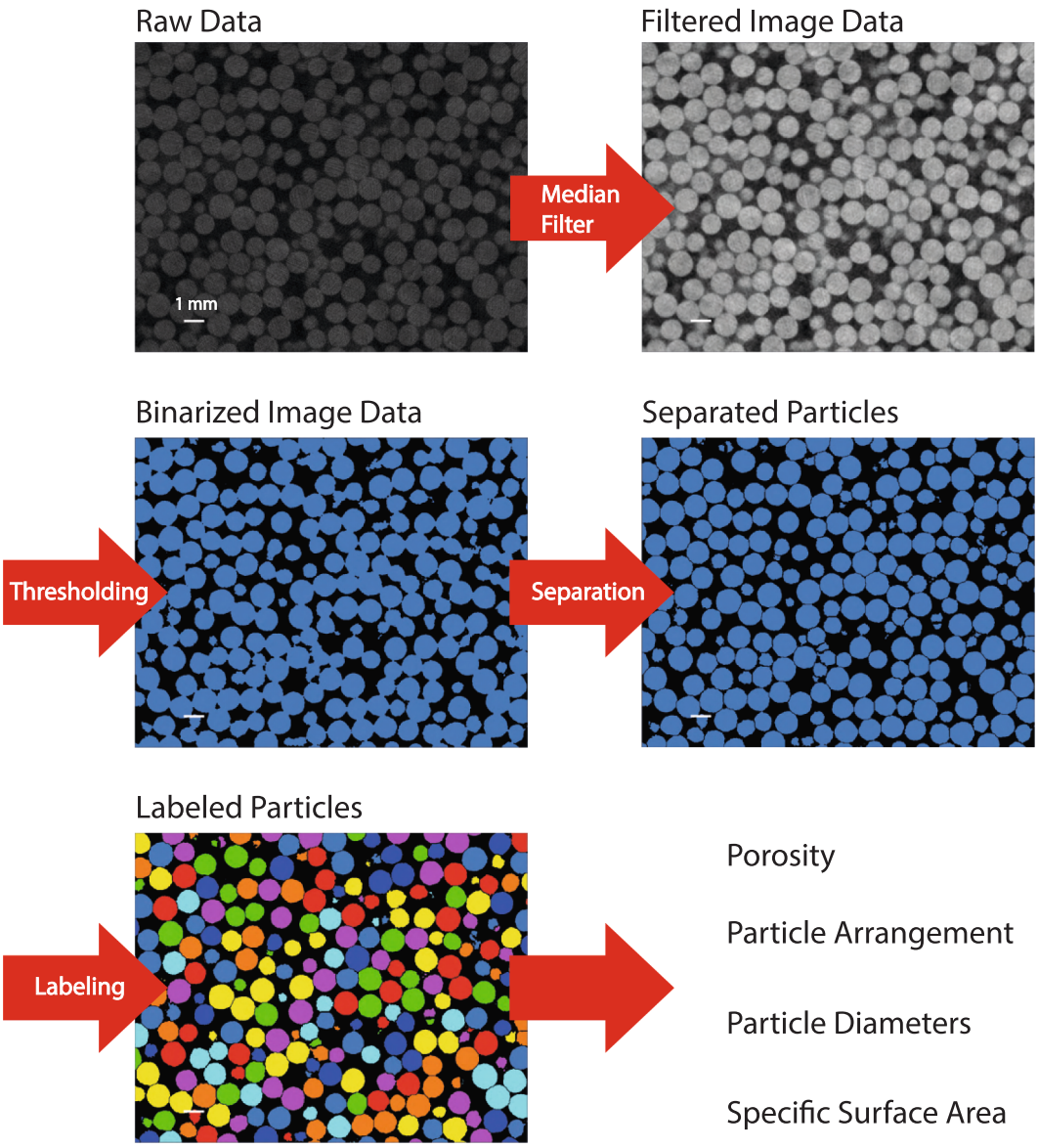

Fig. A1. Process flow chart applied to glass bead specimens (in the labelled phase, the colouring of the particles occurs randomly: after a certain number of beads the colouring is repeated and the same colours are assigned again to different identified objects).

flushed out by the specimen. Because fine particles' diameter is lower than the size of pores and most of the constrictions, most of them are eroded and reach the $y = L$ boundary without deposition. However, the quantity of deposited particles at the end of the test is not constant but slightly increases with y/L.

Finally, in case of G6 ($L \cong 11$ mm), a very large portion of rattlers remains entrapped in the specimen (initially, $Z < 1$, whereas $Z_m \cong 4$) because (i) the *PSD* is sufficiently widely graded and (ii) the volume fraction of small particles is quite large. In contrast to the previous case, not all pores and constrictions are large enough to allow the finer fraction transport. Consequently, in this case, under unsteady conditions, transport and deposition coexist. Only a small fraction of fine particles reaches the $y = L$ boundary (Fig. 5c), while the majority remains clogged in the so-called clogging zones, contributing to force chains' formation (once reached steady state, inside the specimen, $Z \cong 3.5$, whereas $Z_m \cong 4.5$). As anticipated in §1, suffusion leads to a progressive increase in specimen heterogeneity with the alternation of clogging and flushing zones. Based on the numerical test results, to spatially characterise such an alternation, the authors define internal length ℓ_c, as the distance between two adjacent clogging zones. In the present case, $\ell_c =$ 2.1 mm. Owing to the use of selective boundaries along the flow direction, ℓ_c is meant to be independent of both the domain size and the boundary conditions.

A micro-scale variable suitable for describing suffusion processes is u_Y (particle travelling distance along flow direction). In a widely-graded material, u_Y is not constant for any particle (Fig. 6a) and depends on particle diameter D (Fig. 6b, in which $u_{Y,D}$ is the mean u_Y for a given D value, $u_{MAX,D} = \max(u_{Y,D})$ and $D^{\Delta} = \frac{D-D_0}{D_{100}-D_0}$). As is suggested in Fig. 6a, $u_{Y,mean} \cong \ell_c/2$, where $u_{Y,mean}$ is the mean value of u_Y.

By summarizing, (i) in case of G4, the material does not experience suffusion and the specimen remains homogeneous (Fig. 7a and solid light blue line in Fig. 8), (ii) in case of G5, the specimen experiences a suffusion resulting in nearly homogeneous removal of particles (initial and final *PSD* s in Fig. 7b) and the p profile remains almost linear (dashed green line in Fig. 8) and (iii) in case of G6, the specimen experiences suffusion, becomes heterogeneous (initial homogeneous *PSD* and final *PSDs* referred to both flushing and clogging zones are reported in Fig. 7c) and, as a consequence, the p profile becomes non-linear (dashed purple line in Fig. 8).

The same test is also performed on G7 and G8 specimens. The rela-

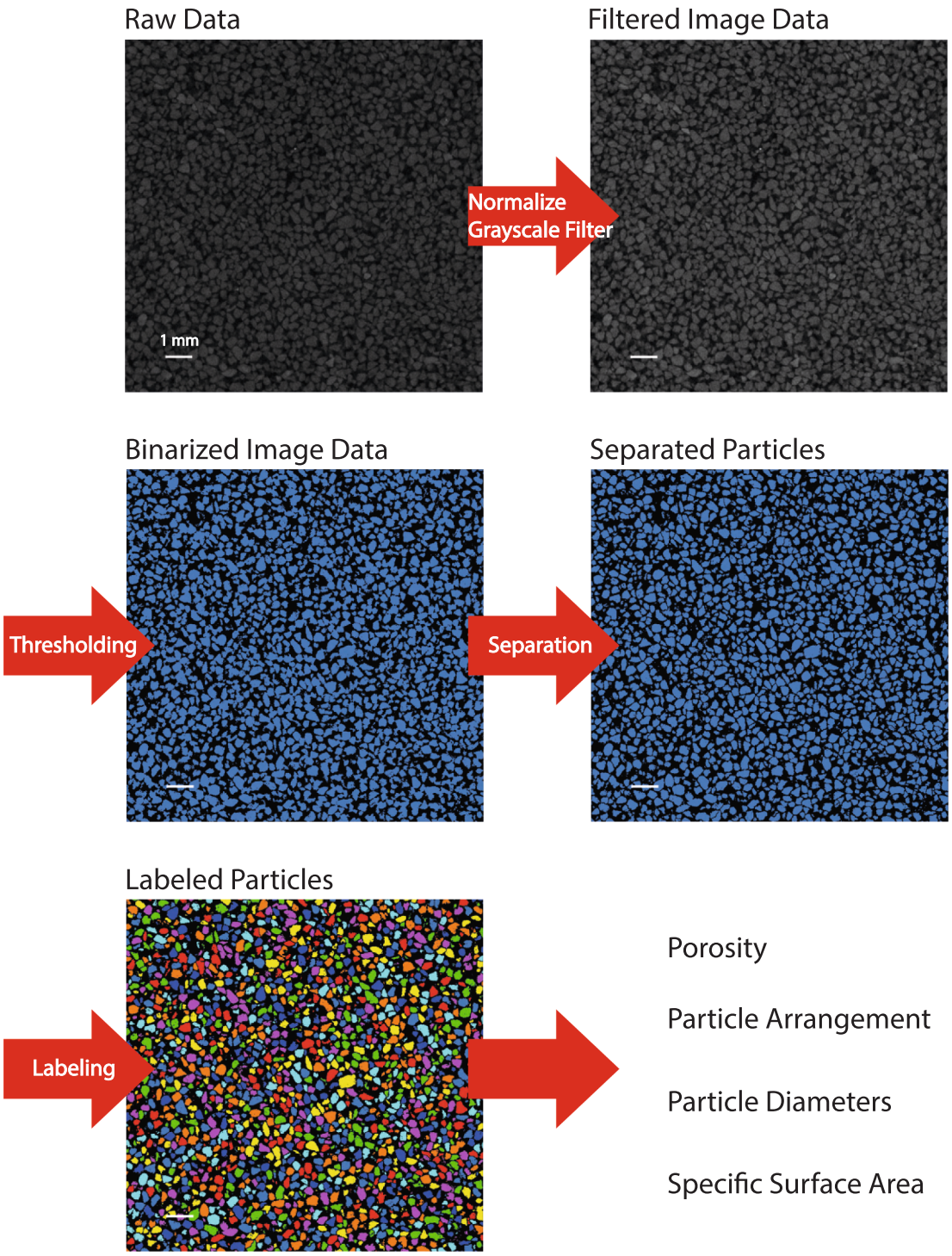

Fig. A2. Process flow chart applied to soil specimens; images of Fossanova sand specimen (in the labelled phase, the colouring of the particles occurs randomly: after a certain number of beads the colouring is repeated and the same colours are assigned again to different identified objects).

tive results are herein omitted for the sake of brevity. G7 specimen does not exhibit suffusion, whereas G8 behaves similarly to G6. In Fig. 6b, $u_{Y,D}/u_{MAX,D}$ versus D^{Δ} curve relative to G8 is also reported. In this normalised plane, G8 and G6 $u_{Y,D}/u_{MAX,D}$ profiles coincide, whereas $u_{MAX,D}$ corresponding to G6 is markedly larger than the one relative to G8.

5.2. The role of σ_0, μ_f and Δp

To study the role of σ_0, μ_f and Δp on the suffusion process, additional numerical tests on G6 specimen (Table 4), for which $\ell_c \ll L$, are performed. Here below, the authors show that σ_0, modifying the material microstructure and in particular initial void ratio e_0, affects the system response at steady state (Fig. 9a), but does not modify the temporal evolution of the process (test T1; dotted black line in Fig. 10). In contrast, μ_f (test T2; Fig. 9b and dotted-dashed grey line in Fig. 10) and Δp (tests T3_0 and T3_1; Fig. 9c-d and dashed grey and black lines in Fig. 10) mainly affect the temporal evolution of suffusion, governing the process rate as long as the macrostructure at steady state.

When σ_0 is varied, ℓ_c does not change, but $u_{Y,fines}$ (which is the mean travelling distance along y direction of fine particles characterised by

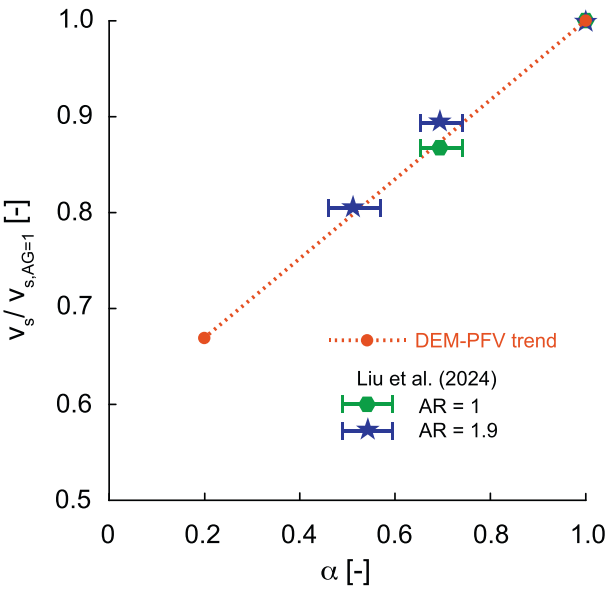

Fig. B1. Initial suffusion rates as a function of the α factor accounting for particle angularity. Each point corresponds to $k = 0.5$, with horizontal error bars representing the variability due to k in the range 0.4–0.6.

$D \leq D_{10}$) is slightly reduced, whereas the temporal evolution of $u_{Yt,fines}/u_{Y,fines}$, where $u_{Yt,fines}$ is the mean value of the travelled distance of fine particles at a given time instant, remains unaltered. The reduction in $u_{Y,fines}$ is mainly the result of the reduction in e induced by the increase in σ_0. In contrast, σ_0 has not a direct influence on $u_{Yt,fines}$ since an increase in σ_0 induces an intensification of already existing force chains, without involving additional fine particles, thus without reducing rattlers available for transport.

Both ℓ_c and $u_{Y,fines}$ are not affected by any change in μ_f, but the time required to reach steady state increases with μ_f. Δp also strongly affects the temporal evolution of the system, by playing an opposite role with respect to μ_f. When Δp is varied, ℓ_c remains unchanged, while $u_{Y,fines}$ exhibits slight variations. The reduction in $u_{Y,fines}$ in test T3_1, indeed, may be justified by observing that higher Δp promotes more frequent collisions and rolling of fine particles during transport, thereby hindering their motion along the flow direction. It is important to note that this effect of Δp pertains specifically to suffusion—defined as the selective removal of finer particles not involved in force chains. Conversely, the onset of other internal erosion mechanisms is influenced by Δp in a more complex manner (Chen et al., 2022).

To better describe the influence of Δp in the suffusion case, the dependence of $F_{fluid,Y}/A_D$ (i.e. y component of mean fluid forces acting upon particles over particles' cross-section area) on D^{Δ} is illustrated in Fig. 11. The curves' shape is governed by (i) the shadow effect of coarser on finer particles and (ii) the non-uniform distribution of local fluid velocity (larger throughout restrictions of the pore matrix, where transported/clogged fine particles are present). The curves are characterised by different shapes according to the more and more prevailing role played by the shadow effect for increasing Δp values.

6. Interpretative simplified method for suffusion inception

As was observed in §5, in case suffusion occurs, initial homogeneous configurations evolve into final steady heterogenous configurations, reached in a time interval mainly ruled by μ_f and Δp (Figs. 5 and 9). Particularly interesting is the dependence of the final stationary state on the initial *PSD* (Fig. 7).

According to the authors, the evolution of the system under the hydraulic perturbation is governed by the local value of *PoS* (§2) and by its spatial distribution. To emphasize it, in Fig. 12a, the temporal evolutions of $PoS - PoS_0$ in G4, G5 and G6 are illustrated. When suffusion does not occur (G4), $PoS - PoS_0$ remains nil (black dashed line). In case of G6, in the flushing zone, PoS_0 monotonically increases (pink lines), whereas, in the clogging zone, the opposite takes place (red lines). The final spatial profile relative to G6 (Fig. 12b) justifies the stability of the new steady-condition, as empirically shown in the literature with reference to granular filter design: the gradient of *PoS* inhibits any subsequent evolution in the *PSD*. When suffusion is severe and transport prevails (G5), $PoS - PoS_0$ increases monotonically all over the domain (green lines), since the entire specimen belongs to the same flushing zone. Even in this case, steady-conditions are stable because of the current spatial distribution of *PoS*.

ℓ_c is introduced by the authors to describe the system response to the hydraulic perturbation. In the numerical results obtained, ℓ_c has been quantitatively assessed only when $\ell_c < L$. This condition is not satisfied in the G5 case, for which ℓ_c, although not infinite, since part of the fine fraction (increasing with y; Fig. 5b) remains trapped within the soil pores, is significantly larger than the simulated domain size. In the light of these results, it can be discussed that more severe suffusion processes at the macro-scale correspond to larger ℓ_c values. When $\ell_c \gg L$, transport process dominates, and the final steady configuration remains relatively homogeneous (Fig. 5b and 7b). Conversely, for $\ell_c < L$, transport and deposition processes coexist. In Fig. 13, ℓ_c is put in relation to PoS_0. The 9 points correspond to the different tests performed on the different specimens, fitted by

$$\frac{\ell_c}{D_{100}} = 1.3 \left\langle \frac{PoS_0}{0.55 - PoS_0} \right\rangle \tag{5}$$

For $PoS_0 \leq 0$, no suffusion is detected and ℓ_c is nil. For $PoS_0 > 0$, higher PoS_0 results in higher ℓ_c. Equation (5) allows to predict the inception of suffusion and to define ℓ_c, an information particularly useful for the interpretation of experimental tests and for predicting the amount of fines eroded during permeation processes.

When suffusion takes place, k stops being constant with time and in space. Here in the following, $\overline{k}(t)$ is defined as the spatial mean value of $k(y,t)$, whereas $\overline{k}_f$ and $\overline{k}_0$ are the final and the initial values, respectively. As shown in Fig. 14, when the entire specimen belongs to the flushing zone (G5), $\overline{k}_f > \overline{k}_0$. In contrast, $\overline{k}_f < \overline{k}_0$ when transport and deposition coexist (G6). Finally, in Fig. 15, the temporal evolutions of $\overline{k}/\overline{k}_0$ during the different erodimetric tests upon G6 specimen are illustrated. When transport takes place, but deposition is not yet occurring, a very rapid increase in $\overline{k}$ is observed. Subsequently, when fine particles deposit and the system becomes heterogeneous, $\overline{k}$ reaches $\overline{k}_f$. The time required to reach steady conditions as well as the peak value of $\overline{k}$ are affected by Δp, μ_f, whereas $\overline{k}_f$, as expected, does not.

7. Concluding remarks

In this paper, a discontinuum numerical approach has been applied to simulate permeation in sands accounting for suffusion processes. The novelty of this work lies in (i) the discussion of the role of sand particles' angularity in influencing material intrinsic permeability leading to the development of a simplified method for its numerical assessment, (ii) the theoretical comprehension of suffusion-related processes (transport and deposition) and (iii) the introduction of an interpretative approach potentially useful for practical predictions.

A non-dimensional coefficient α is proposed to approximate angularity effects in DEM-coupled simulations using spheres, without explicitly modelling the full geometric complexity of real particles. In such a context, the use of this shape descriptor allows for a reasonable compromise between physical realism and numerical efficiency.

Unsteady conditions associated with suffusion, which lead to spatial and temporal variations in intrinsic permeability, are then studied

numerically by simulating erodimetric tests. The particle size distribution (*PSD*) is found to play a crucial role in governing suffusion inception. Starting from an initial homogeneous state, the system evolves towards a stable heterogeneous state, which is primarily influenced by the initial *PSD*. This transition occurs in a time interval depending on fluid viscosity and imposed hydraulic gradient.

The state variable governing suffusion in granular media, identified in this study, is the POtential to Suffusion *PoS*, which represents the non-dimensional area between the *PSD* curve and the straight line intersecting it at D_0/D_{100} and 1. The initial *PoS* value allows to predict the occurrence of suffusion and to quantify ℓ_c, i.e. the wavelength of the suffusion-induced heterogeneity. The *PoS* spatial distribution, that is its local gradient, is crucial for the stability of the final steady state. Evaluating the initial *PoS*, and thus ℓ_c, appears to be a helpful tool for interpreting experimental test results, as it can support the prediction of eroded fines (depending on the sample length relative to ℓ_c), and the observation of hydraulic conductivity evolution during permeation.

CRediT authorship contribution statement

Katia Boschi: Writing – original draft, Methodology, Conceptualization, Writing – review & editing, Visualization, Investigation. **Bruno Chareyre:** Writing – review & editing, Methodology, Supervision. **Claudio di Prisco:** Writing – review & editing, Methodology, Supervision.

Declaration of competing interest

The authors declare that they have no known competing financial interests or personal relationships that could have appeared to influence the work reported in this paper.

Acknowledgements

This research has been supported by MBS Master Builders Solutions Italia S.p.A. within a research program aimed at both investigating and modelling the coupled hydromechanical processes governing grout injections. The authors gratefully acknowledge Dr. Davide Grassi and Dr. Nicoletta Fusi for their valuable support during the laboratory phase.

Appendix A:. Micro-CT scanning and image post-processing

The micro-CT device used for imaging of granular specimens is BirACTIS 130/150 device of the laboratory of the DISAT department at Bicocca University (Milan, Italy). The measurement parameters for the investigated scans are 120 kV and 100 μA. 2160 views per rotations are averaged three by three. The voxel resolution of the microCT scans remains constant and equal to 20 μm (i.e. 0.02 mm × 0.02 mm × 0.02 mm).

3D reconstruction of 2D slices obtained from microCT technique is carried out by means of Avizo (Mercury) software. Figs. A1 and A2 show the main image processing steps applied to both glass bead and soil specimens. The image is interpreted and processed as a three-dimensional volume and the grey-values of each voxel are numbers of decimals obtained from 16-bit binary representation of the grey level. The grey-scale distribution of the raw data shows two peaks which can be clearly attributed to (i) pore space and (ii) solid matrix.

The raw image file is first filtered. The grey values belonging to a few image bright spots (often caused by either density fluctuations or chemical impurities) are lowered artificially by setting a defined maximum threshold. Additionally, in the case of glass bead specimens, the so-called “Median” filter, applied to de-noise and smooth the image data, is sufficient. This filter uses morphological operators to set the grey-scale value of a voxel to the median for a defined neighbourhood (26 voxels with at least one common vertex are considered connected). In contrast, in the case of soil specimens, since the grey-scale values belonging to solid matrix and pore space overlap due to their wide distributions, the so-called “Normalise greyscale” filter is applied to enhance the edges of the soil particles and to adjust the contrast between pore space and solid one.

Then, the filtered grey-scale image data are “thresholded” to generate a binarized image data. The threshold is selected manually for each specimen in a way that the solid particles are assigned to values of unity and the pore space voxels are set to zero. A good agreement with the experimentally determined global porosities proves the correctness of the filtering and segmentation procedure performed.

For obtaining information referred to the solid phase, the segmented particles are separated by employing a high-level combination of watershed, distance transform and numerical reconstruction algorithms. The separated particles are then numerated by means of the “labelling” module; i.e. each voxel of the same object is assigned to the same value and each object gets a different value. Based on the labelled system, a quantitative analysis is performed to determine (i) the volume-equivalent diameter of each particle object, (ii) the three-dimensional values of particle volume and surface area and (iii) the barycentre position of each particle with respect to a provided system of reference. A satisfactory agreement with the particle size distributions obtained from the common laser diffraction particle-size analyser proves the correctness of the method employed.

Appendix B:. Validation of the proposed simplified strategy for including particle angularity effects in DEM-coupled modelling

A simplified numerical strategy to account for particle angularity (*AG*) in DEM-coupled simulations, while avoiding the explicit representation of complex particle geometries, is proposed in §5, based on the conclusions drawn in §4. The method consists in replacing fluid viscosity μ_f with an effective (fictitious) viscosity, defined as μ_f/α. The validity of this approach is assessed here by comparing the suffusion rates obtained using this strategy with those reported by Liu et al. (2024), who employed a fully resolved DEM-CFD model incorporating irregularly shaped particles.

In Fig. 11 of Liu et al. (2024), suffusion rates for different granular packings with varying both *AR* and *AG* are reported. In their study, the aspect ratio is defined as $AR = c/a$, where c and a are the semi-major and semi-minor axes of prolate ellipsoids, respectively. Angularity is quantified as $AG = d_{2-8}/d_1$, where d_1 is the first-order spherical harmonic norm of the best-fitting ellipsoid, and d_{2-8} captures higher-order geometric deviations from ellipsoidal symmetry (related to edges and corners). For the simulated packings, the α factor accounting for angularity alone is given by $S^2_{0,AR}/S^2_{0,AR-AG}$ where $S_{0,AR-AG}$ is the specific surface area of the packing with a given *AR* and *AG*, and $S_{0,AR}$ the specific surface area of a reference packing with the same *AR* but $AG = 1$. Under the assumption that angularity increases surface area without significantly altering volume and in agreement with Chhabra (2007), $S_{0,AR-AG} = S_{0,AR} \bullet (1 + k \bullet AG)$, where k is a dimensionless angularity amplification coefficient and *AG* is evaluated in agreement with Liu et al. (2024). Experimental studies on natural and crushed sands (Cho et al., 2006; Wang & Vallejo, 2015) suggest values of k in the range 0.4–0.6. Consequently, $\alpha = 1/(1 + k \bullet AG)^2$.

This formulation allows initial suffusion rates v_s from Liu et al. (2024) to be re-plotted as a function of α, as shown in Fig. B1. In particular, v_s values

are reported as normalized ratios $v_s/v_{s,AG=1}$, with $v_{s,AG=1}$ being the reference suffusion rate for $AG = 1$. For the two cases $AR = 1$ and $AR = 1.9$ investigated by Liu et al. (2024), representative of natural and industrial sands, their trends show close agreement with the one obtained in the present study for different values of viscosity assigned in the DEM-PFV simulations (for a fixed fluid viscosity $\mu_f = 1$ mPa• s, the assigned value is given by μ_f/α). Given the satisfactory agreement observed, the authors consider the proposed strategy to be a reliable and practical approach for $AR < 2$.

Data availability

Data will be made available on request.

References

Angelidakis, V., Boschi, K., Brzeziński, K., Caulk, R.A., Chareyre, B., del Valle, C.A., Thoeni, K., 2024. YADE-an extensible framework for the interactive simulation of multiscale, multiphase, and multiphysics particulate systems. Comput. Phys. Commun. 109293. https://doi.org/10.1016/j.cpc.2024.109293.

Bilotta, E., Casale, R., Di Prisco, C. G., Miliziano, S., Peila, D., Pigorini, A., & Pizzarotti, E. M. (2022). Handbook on Tunnels and Underground Works: Volume 1: Concept–Basic Principles of Design. CRC Press.

Bonelli, S., 2013. Erosion in geomechanics applied to dams and levees. John Wiley & Sons.

Bonilla, R.R.O., 2004. Numerical simulation of undrained granular media. University of Waterloo. PhD thesis.

Boschi, K., 2021. Permeation grouting in granular materials. From micro to macro, from experimental to numerical and viceversa. Politecnico di Milano (Italy). PhD thesis.

Boschi, K., Grassi, D., Castellanza, R.P., di Prisco, C.G., 2023a. Permeation grouting in soils: Numerical discussion of a simplified analytical approach. In: Proceedings of the Institution of Civil Engineers-Ground Improvement, pp. 1–9.

Boschi, K., di Prisco, C., Grassi, D., 2023b. Design of Permeation Grouting Treatments with Eco-Friendly Nanosilica Grouts. In: National Conference of the Researchers of Geotechnical Engineering. Cham, Springer Nature Switzerland, pp. 621–628.

Boschi, K., di Prisco, C.G., Grassi, D., Modoni, G., Salvatore, E., 2024. Nanosilica grout permeation in sand: experimental investigation and modeling. J. Geotech. Geoenviron. Eng. 150 (1), 04023129.

Cao, Z., Xiao, Z., Cai, Y., Han, J., 2024. Investigation of suffusion in soil with arching based on CFD–DEM simulation. Int. J. Geomech. 24 (3), 04024014.

Carman, P.C., 1937. Fluid flow through granular beds. Trans Inst Chem Eng London 15, 150–166.

Catalano, E., Chareyre, B., Cortis, A., Barthélémy, E., 2011. A pore-scale hydro-mechanical coupled model for geomaterials. In: In PARTICLES II: Proceedings of the II international conference on particle-based methods: Fundamentals and applications, pp. 798–809.

Catalano, E., Chareyre, B., Barthélemy, E., 2014. Pore-scale modeling of fluid-particles interaction and emerging poromechanical effects. Int. J. Numer. Anal. Meth. Geomech. 38 (1), 51–71. https://doi.org/10.1002/nag.2198.

Chang, D., Zhang, L., 2011. A stress-controlled erosion apparatus for studying internal erosion in soils. Geotech. Test. J. 34 (6), 579–589.

Chapuis, R.P., 2012. Predicting the saturated hydraulic conductivity of soils: a review. Bull. Eng. Geol. Environ. 71, 401–434. https://doi.org/10.1007/s10064-012-0418-7.

Chareyre, B., Cortis, A., Catalano, E., Barthélemy, E., 2012. Pore-scale modeling of viscous flow and induced forces in dense sphere packings. Transp. Porous Media 94, 595–615. https://doi.org/10.1007/s11242-012-0057-2.

Chen, T., Hu, Z., Yang, Z., Zhang, Y., 2023a. A resolved CFD–DEM investigation into the onset of suffusion: effect of confining pressure and stress anisotropy. Int. J. Numer. Anal. Meth. Geomech. 47 (16), 3018–3043.

Chen, F., Xiong, H., Wang, X., Yin, Z.Y., 2023b. Transmission effect of eroded particles in suffusion using the CFD-DEM coupling method. Acta Geotech. 18 (1), 335–354.

Chhabra, R.P., 2007. Bubbles, Drops, and Particles in Non-Newtonian Fluids, 2nd ed. CRC Press, Boca Raton, FL.

Cho, G.-C., Dodds, J., Santamarina, J.C., 2006. Particle shape effects on packing density, stiffness, and strength: Natural and crushed sands. J. Geotech. Geoenviron. Eng. 132 (5), 591–602. https://doi.org/10.1061/(ASCE)1090-0241(2006)132:5(591).

Cundall, P., Strack, O., 1979. A discrete numerical model for granular assemblies. Geotechnique 29, 47–65.

Darcy, H. (1856). Les fontaines publiques de la ville de Dijon: exposition et application des principes à suivre et des formules à employer dans les questions de distribution d'eau (Vol. 1). Victor dalmont. Paris: Dalmont.

Hakuno, M., 1995. Simulation of the dynamic liquefaction of sand. In: Earthquake Geotechnical Engineering. Balkema, Rotterdam, pp. 857–862.

Hosn, R., Sibille, L., Benahmed, N., Chareyre, B., 2017. Discrete numerical modeling of loose soil with spherical particles and interparticle rolling friction. Granul. Matter 19, 1–12. https://doi.org/10.1007/s10035-016-0687-0.

Hu, Z., Zhang, Y., Yang, Z., 2019. Suffusion-induced deformation and microstructural change of granular soils: a coupled CFD–DEM study. Acta Geotech. 14, 795–814.

Hu, Z., Zhang, Y., Yang, Z., 2020. Suffusion-induced evolution of mechanical and microstructural properties of gap-graded soils using CFD-DEM. J. Geotech. Geoenviron. Eng. 146 (5), 04020024.

Ke, L., Takahashi, A., 2012. Strength reduction of cohesionless soil due to internal erosion induced by one-dimensional upward seepage flow. Soils Found. 52 (4), 698–711. https://doi.org/10.1016/j.sandf.2012.07.010.

Ke, L., Takahashi, A., 2014. Experimental investigations on suffusion characteristics and its mechanical consequences on saturated cohesionless soil. Soils Found. 54 (4), 713–730.

Kenney, T.C., Lau, D., 1986. Internal stability of granular filters: Reply. Can. Geotech. J. 23 (3), 420–423. https://doi.org/10.1139/t86-068.

Kézdi, Á., 2013. Soil physics: selected topics. Elsevier, Amsterdam, The Netherlands.

Kozeny, J., 1927. Ueber kapillare Leitung des Wassers in Boden. Sitzungsber Akad, Wiss., Wien Math. Naturwiss. Kl. Abt. 2a 13, 271–306.

Liu, Y., Wang, L., Yin, Z.Y., Hong, Y., 2023. A coupled CFD-DEM investigation into suffusion of gap-graded soil considering anisotropic stress conditions and flow directions. Acta Geotech. 18 (6), 3111–3132.

Liu, Y.J., Yin, Z.Y., Huang, S., Lai, Z., Zhou, C., 2024. Resolved CFD-DEM modeling of suffusion in gap-graded shaped granular soils. J. Geotech. Geoenviron. Eng. 150 (4), 04024008.

Marot, D., Rochim, A., Nguyen, H.H., Bendahmane, F., Sibille, L., 2016. Assessing the susceptibility of gap-graded soils to internal erosion: proposition of a new experimental methodology. Nat. Hazards 83, 365–388. https://doi.org/10.1007/s11069-016-2319-8.

O'Sullivan, C. (2011). Particulate discrete element modelling: a geomechanics perspective. CRC Press. London, UK. https://doi.org/10.1201/9781482266498.

Scheidegger, A.E., 1957. The physics of flow through porous media. University of Toronto press.

Smilauer, V., Angelidakis, V., Catalano, E., Caulk, R., Chareyre, B., Chevremont, W., ... & Yuan, C. (2023). Yade documentation. arXiv preprint arXiv:2301.00611.

Scholtes, L., Hicher, P.Y., Nicot, F., Chareyre, B., Darve, F., 2009. On the capillary stress tensor in wet granular materials. Int. J. Numer. Anal. Methods Geomech. 33 (10), 1289–1313.

Sterpi, D., 2003. Effects of the erosion and transport of fine particles due to seepage flow. Int. J. Geomech. 3 (1), 111–122. https://doi.org/10.1061/(ASCE)1532-3641(2003)3:1(111).

Suhr, B., Six, K., 2016. On the effect of stress dependent interparticle friction in direct shear tests. Powder Technol. 294, 211–220. https://doi.org/10.1016/j.powtec.2016.02.029.

To, P., Scheuermann, A., Williams, D.J., 2018. Quick assessment on susceptibility to suffusion of continuously graded soils by curvature of particle size distribution. Acta Geotech. 13, 1241–1248. https://doi.org/10.1007/s11440-017-0611-8.

Tong, A.T., Catalano, E., Chareyre, B., 2012. Pore-scale flow simulations: model predictions compared with experiments on bi-dispersed granular assemblies. Oil & Gas Science and Technology-Revue d'IFP Energies nouvelles 67 (5), 743–752.

Valdes, J.R., Santamarina, J.C., 2006. Particle clogging in radial flow: Microscale mechanisms. SPE J. 11 (02), 193–198.

Wang, Y.H., Vallejo, L.E., 2015. Characterization of particle shape using Fourier descriptors and correlation with shear strength of granular materials. Eng. Geol. 183, 1–10. https://doi.org/10.1016/j.enggeo.2014.09.009.

Wautier, A., Bonelli, S., Nicot, F., 2019. DEM investigations of internal erosion: Grain transport in the light of micromechanics. Int. J. Numer. Anal. Meth. Geomech. 43 (1), 339–352. https://doi.org/10.1002/nag.2866.

Wyllie, M.R.J., Gardner, G.H.F., 1958a. The generalized Kozeny-Carman equation. Part 1. Review of existing theories. World Oil 146 (5), 121–128.

Wyllie, M.R.J., Gardner, G.H.F., 1958b. The generalized Kozeny-Carman equation. Part 2. A novel approach to problems of fluid flow. World Oil 146 (5), 210–228.

Zhong, C., Le, V.T., Bendahmane, F., Marot, D., Yin, Z.Y., 2018. Investigation of spatial scale effects on suffusion susceptibility. J. Geotech. Geoenviron. Eng. 144 (9), 04018067.